

LA-UR-21-25952

Approved for public release; distribution is unlimited.

Title: Design of the New DARHT X-ray and Neutron Shielding and Measured Results

Author(s): Mendez, Albert Jacob
Salazar, Gary P.
Pickrell, Mark Manley

Intended for: Report

Issued: 2021-06-24

Disclaimer:

Los Alamos National Laboratory, an affirmative action/equal opportunity employer, is operated by Triad National Security, LLC for the National Nuclear Security Administration of U.S. Department of Energy under contract 89233218CNA000001. By approving this article, the publisher recognizes that the U.S. Government retains nonexclusive, royalty-free license to publish or reproduce the published form of this contribution, or to allow others to do so, for U.S. Government purposes. Los Alamos National Laboratory requests that the publisher identify this article as work performed under the auspices of the U.S. Department of Energy. Los Alamos National Laboratory strongly supports academic freedom and a researcher's right to publish; as an institution, however, the Laboratory does not endorse the viewpoint of a publication or guarantee its technical correctness.

Design of the New DARHT X-ray and Neutron Shielding and Measured Results

A. Jacob Mendez, Gary P. Salazar, Mark M. Pickrell

June 16, 2021

I. Introduction, Background, and Baseline

The DARHT Weather Enclosure (WE) project provided an excellent opportunity to redesign and rebuild some of DARHT systems without introducing interruptions to normal operations. Multiple improvements were made to the facility to improve data quality and operational reliability. Some of these were simple, such as replacing cables and hardware. However, one of the most important was implementing the Variable Field of View (VFoV), which enables DARHT to make simultaneous measurements of an imploding pit and also the surrounding case. One view has the typical DARHT focus and conjugate ratios, and the other view has moved the both the source and Gamma-Ray Cameras (GRC) so that a much larger view is possible. The VFoV provides a unique capability and physics improvement to DARHT. Further, the Weather Enclosure will improve GRC measurements by maintaining the cameras at a near constant temperature, which reduces the bias drift of the detectors. However, the Weather Enclosure and many of these improvements imposed operational constraints at the DARHT firing point. Two that affected the GRC camera measurements were that the available space was significantly constrained and the GRC houses needed to be moveable. The original GRC houses were built and installed for use in open air firing of DARHT Hydrotests, without a confinement vessel. Therefore, the GRC houses were constructed of steel blast enclosures that protected the cameras and sensitive electronics from fragments and explosive shock. These steel enclosures provided ancillary benefits as well: the thick steel was an excellent shield against electro-magnetic interference (EMI) and also stray gamma-ray radiation. Thus, the radiation shielding was built in. However, these thick enclosures were heavy, quite large and essentially fixed in place therefore, they could not work in the new Weather Enclosure and VFoV context. New GRC enclosures were designed, built, and installed in the DARHT Weather Enclosure. These were much lighter than the originals, and were designed to provide EMI and visible light shielding only. As such, they could be moved to accommodate both the reassembly of DARHT and VFoV applications. The primary gamma ray and neutron shielding had to be provided separately. The shielding also had to be configured so that it could be disassembled and moved. The conceptual design called for using concrete blocks (as with the original DARHT shielding) and a semi-enclosure (called the steel-poly wall), which provided additional neutron and gamma-ray shielding. The steel-poly wall, as its name suggests, used steel, high density polyethylene (HDPE), and borated polyethylene to shield against both neutrons and gamma rays. Similarly, the concrete blocks also provided shielding against both neutrons and gamma rays.

The new radiation shields were heavily constrained. We had two objectives to this study and implementation of the neutron and gamma-ray shielding, within the operational constraints of the WE:

- Implement neutron and gamma-ray shielding that at a minimum achieves the same level of protection against neutrons and gamma-rays as the original, heavy steel, gamma-ray camera enclosures.
- Experimentally determine the pathways for radiation interference, so that the shielding may be incrementally improved in the future.

Stray neutrons, or gamma-ray photons that are outside of the direct radiographic image cone, cause bright, single pixel events or “stars” in the image and also contribute to the general noise background, which degrades the radiographic image quality. While the stars can be removed from the image using standard image processing algorithms, efforts to minimize them serve to improve overall image quality and reduce scattered radiation dose to sensitive camera head electronics. Both effects degrade the quality of the image and make it harder to quantitatively analyze the image using the Bayesian Inference Engine (BIE) software system. However, for this study, we found that counting the “stars” in a GRC image provided the most effective and direct measure of the effects of radiation interference. That measurement will be used in this report as the quantitative measure of image quality; specific radiographs will be processed to create “star masks” that will be shown here. These mask provide a quantitative measure of “stars” in the image.

The DARHT accelerators produce intense forward directed X-ray beams via Bremsstrahlung X-ray production. In order to minimize scattered radiation, the forwarded directed beams are collimated and shielded using Tungsten and other materials. However, limited space around the X-ray source restricts the amount of shielding that can be used. As a consequence, a measureable portion of the X-ray beam, outside the acceptance angle of the collimation, will reach the detector plane. This flux travels outside of the direct beamline, but can subsequently enter the Gamma-Ray Camera (GRC) enclosures through Compton scattering. The Compton-scattered photons may have sufficient residual energy that they can interfere with the electronics of the Gamma-Ray camera charge coupled devices (CCD’s) themselves, or with the X-ray scintillator. Stray neutrons are also produced by the powerful DARHT accelerators. Almost all are generated in the accelerator target regions. The dominant process is photo-neutron production, where a high energy X-ray interacts with a bound neutron in a typically high-Z material and knocks the neutron out of the nucleus. The common reaction is the Giant Dipole Resonance (GDR). [1]

There are two mechanisms for image degradation by stray neutrons and X-ray photons that we consider:

- Single event upsets of the camera electronics and detector. This process has been widely investigated because of the deleterious effects on electronics operation. It is nominally caused by ionizing radiation, such as X-rays. However, neutron interactions, particularly neutron absorption in the Boron doping of semiconductors, can also produce an ionization trail. [2, 3] In addition, charged particles, generated from x-ray interaction is surrounding materials can also produce charge trails in the CCD.
- Similarly, absorption of Compton-scattered X-ray photons in the GRC scintillator material can provide a significant additive signal to direct X-ray photons.

These processes can cause both the “stars” in the radiographic images and also contribute to the general noise background. Therefore, shielding against this stray radiation is an essential part of maintaining and improving DARHT radiographic quality.

II. Design Studies of Neutron and Gamma Shielding

A. Neutron Shielding Principles

Our initial efforts to mitigate scattered radiation was based on established and accepted shielding designs followed by an MCNP study.[4] The general design for an optimum shield, for both neutrons and gamma rays, is based on the underlying physics of neutron and gamma-ray scattering. Common designs have emerged over the years as the physics drives the designs in a particular direction.

Neutron scattering is primarily by two processes: inelastic scattering and neutron absorption. Inelastic scattering means that energy and momentum are conserved between the incident neutron and the target nucleus; there is no gamma ray emitted. With each collision, the energy is partitioned between the incident neutron, which is typically at high energy (e.g. ~1MeV), and the target nuclei, which may be at actual room temperature (e.g. 0.025eV). Therefore, the neutron will lose energy with each collision, which is a process

called moderation. The process is governed by ordinary Newtonian kinematics, therefore, the most effective nucleus for moderation is one with the identical mass as the neutron, which is simply hydrogen. Therefore, the most effective mechanism for neutron moderation (i.e. reducing the incident neutron energy to nominally room temperature) is to use the highest possible concentration of hydrogen as possible. The two materials that provide the highest hydrogen density are ordinary water (H₂O), and a simple, industrial plastic called high density polyethylene (HDPE), (CH₂).

Neutron absorption is an entirely different process, and involves specific isotopes that have a large neutron absorption cross section. Examples are ¹⁰Boron and ¹¹³Cadmium. The absorption cross section varies inversely with incident neutron energy, with the largest values at the lowest energies. The boron and cadmium absorption cross sections are shown below in Figure 1.

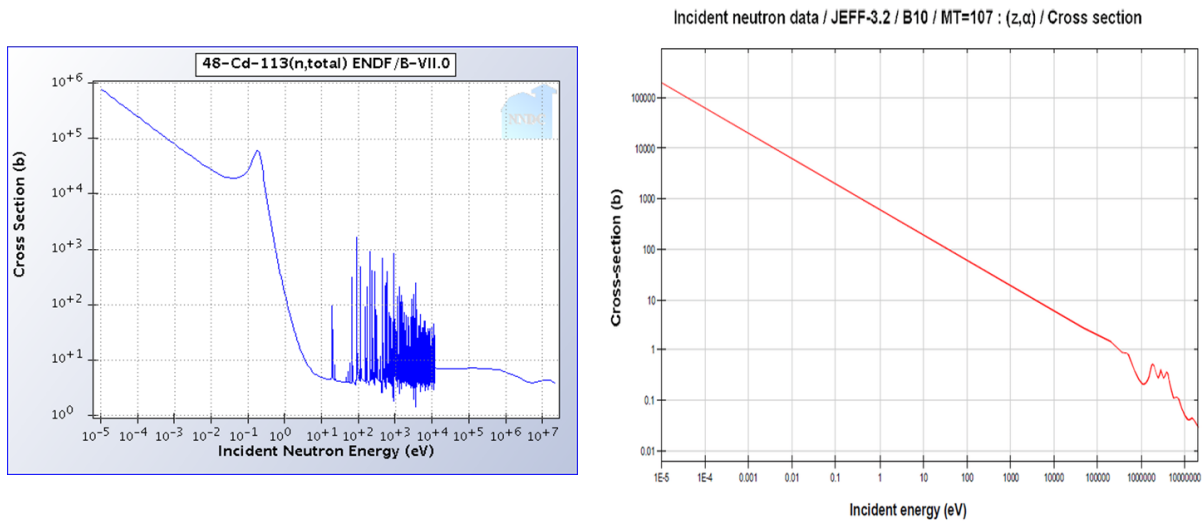


Figure 1: Scaling of the absorption cross section for both ¹¹³Cd and ¹⁰B as a function of incident neutron energy. Note that in all cases, the absorption cross section increases as neutron energy decreases. The maximum achievable cross section occurs at room temperature (0.025 eV).

The total absorption cross section, Σ , will scale as the cross section for the individual nucleus, σ , times the nuclei density, n :

$$\Sigma = n\sigma = \frac{\sigma\rho N_A}{A} \quad (1)$$

Where ρ is the material density, A is the atomic weight and N_A is Avogadro's number. For pure boron and cadmium, in units of barns / cm³, the values are:

Cadmium: 344 Boron: 4.8

The net effect of this physics is shown in the schematic diagram below in Figure 2. As is seen from the plots in Figure 1 above, the absorption cross section for incident neutrons is very small for both cadmium and boron for high energies (i.e. the typical energies that neutrons are “born” at in nuclear processes). Therefore, if a neutron absorber is placed near the incident surface of a radiation shield, it will have very little beneficial effect. The absorption cross section is just too small at these energies. However, the average neutron energy is much smaller after several collisions with hydrogen, so that the absorption is much more effective after a few inches of hydrogen-bearing material. The cadmium absorber shown in Figure 2 is placed at the back end of the HDPE block, where it will be much more effective. So, rather than using

borated polyethylene, which reduces the hydrogen concentration, is it more effective to use pure HDPE and follow it with either boron or cadmium at the back end.

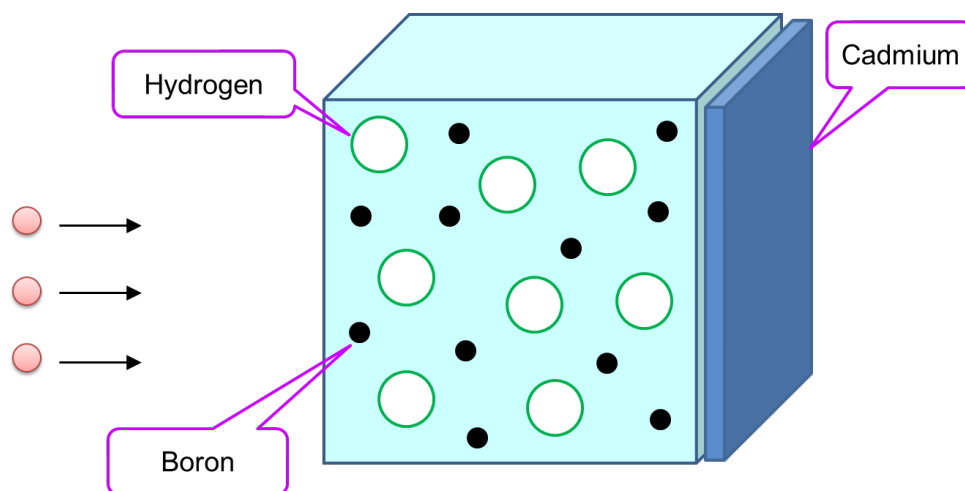


Figure 2: Schematic of a simple neutron shield.

B. Gamma Shielding Principles

Gamma-ray shielding is mostly based on two processes where incident gamma-rays (or X-rays) interact with bound electrons. These are Compton Scattering and the Photoelectric Effect. The relative cross sections for Compton Scattering, the Photoelectric Effect, Pair Production, and the sum of all these processes, are shown below in Figure 3. Below about 100 keV, the photoelectric process dominates. From 100 keV to 10 MeV, the Compton scattering process dominates, and above 10 MeV, the pair production process dominates. The X-ray photons produced by the DARHT accelerators are typically a few to 10 MeV, so that the Compton scattering process is initially dominant. Moreover, from a shielding perspective, once photons are scattered to low energies such that the photoelectric process is dominant, the cross sections become huge and the shielding much simpler to implement. Therefore, we will focus on the Compton Scattering process.

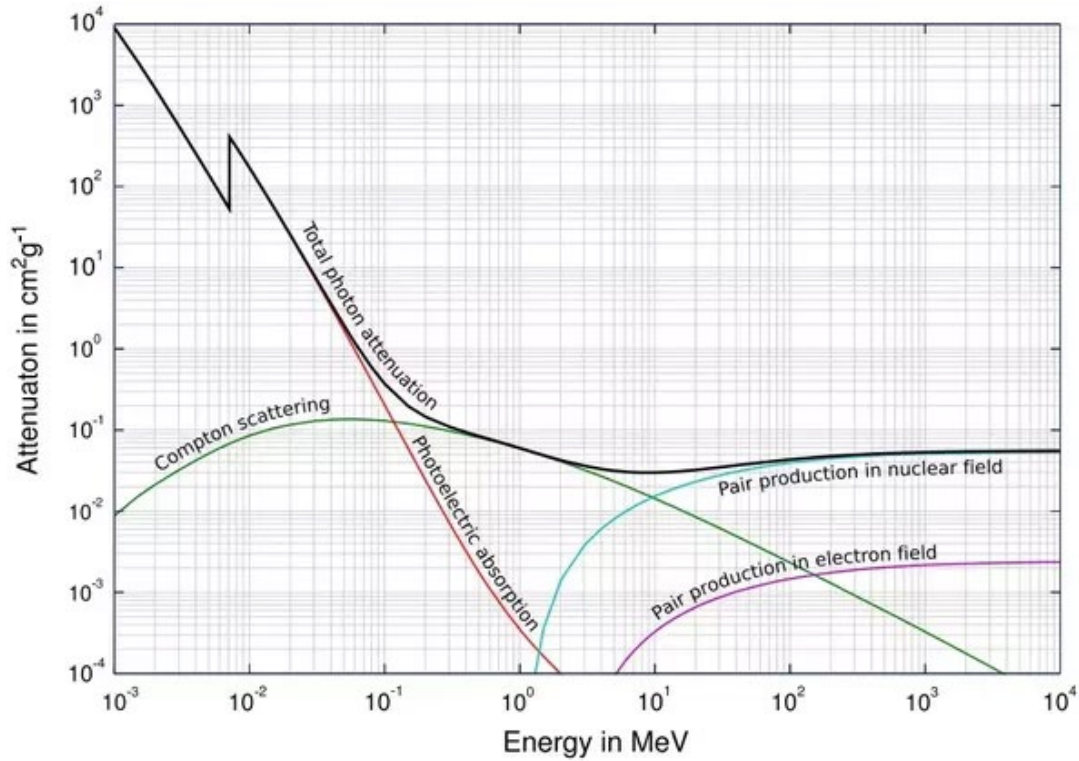


Figure 3: Plot of the cross sections for the Photoelectric, Compton scattering, and Pair production mechanisms for X-ray (or gamma ray) interaction with electrons. The electrons are typically bound, and must be bound for the Photoelectric effect. The total cross section is also shown as the sum. At low energies ($E < 100$ keV) the Photoelectric effect dominates. At energies between 100 keV and 10 MeV, Compton scattering dominates. At energy above 10 MeV, Pair production dominates. [5]

The over-all Compton cross section is proportional to the density of bound electrons in the shielding material, and is best parameterized by the linear attenuation coefficient:

$$I(x) = I_0 \exp(-\mu x) \quad (2)$$

where μ is the linear attenuation coefficient and I is intensity

The value of μ depends on the Compton cross section, σ , and the density of electrons:

$$\mu = n_e \sigma = \frac{\sigma \rho N_A Z}{A} \quad (3)$$

Where, as before, σ is the Compton cross section, ρ is the material density, A is the atomic mass, Z is the atomic number, and N_A is Avogadro's number. The conclusion from equation (3) and the cross section plots in Figure 3 above is that the most effective gamma-ray (X-ray) shielding materials will be those with high atomic number and high specific gravity. Lead and tungsten are excellent. However, more ordinary materials such as steel or iron are still very good.

The final physics consideration for the shielding design is that high energy (gamma-ray) photons can produce neutrons through the photo neutron process. The cross section is quite small and was not included in Figure 3 above, but it is sufficiently large that it should be considered. Conversely, the absorption of neutrons by either boron or cadmium releases a capture gamma ray. Thus, the shielding problem is interconnected: shielding of neutrons produces a small gamma-ray flux, and shielding of gamma rays produces a small neutron flux. Therefore, the overall shielding design must integrate methods to attenuate

both fluxes. For the MCNP studies we conducted, the general design is shown in Figure 4 below. The distribution between the materials was optimized in MCNP to minimize the combined neutron and gamma flux. Due to supply chain delays and schedule restraints the optimized shielding design in Figure 5 was not implemented for this study. Rather, a design that adopted many of the features of the optimized design with materials that were more readily available was implemented. This design utilized two inches of High Density Polyethylene, one inch of Borated Poly, one inch of Poly Bismuth, one eight inch of Flexible Boron and two inches of Steel. Unfortunately due to supply chain issues and schedule constraints, the Poly Bismuth was replaced with an additional inch of Borated Poly. The Poly Bismuth is particularly desirable because in addition to good neutron moderation it is also very effective as a photon shield, as one inch of this material is equivalent to one quarter inch of lead. The final implementation of the GRC shields, shown in Figure 9, utilized different materials than the optimized design, but the general physics principles were retained. In the final design, steel replaced lead and borated polyethylene replaced cadmium. For the shielding of the accelerator target chambers, only neutron shielding was implemented, but it used the exact configuration of HDPE followed by a sheet of cadmium.

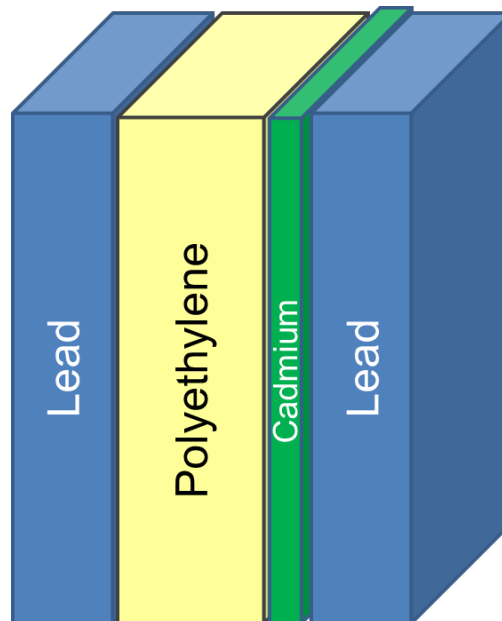


Figure 4: Schematic depiction of the optimized shielding design that was used for the MCNP calculations for the shielding of the GRC enclosures. The MCNP calculations for the target boxes only included the neutron shielding components. The choice of materials is somewhat notional, in that other materials could be substituted for ease in construction.

C. MCNP Studies

1. Target Chamber

MCNP studies were used to optimize the shielding design. Starting from the basic theoretical considerations and representative designs discussed above in sections II.A and II.B. The target chamber design was optimized using HDPE and cadmium. The target chamber is a very complicated geometry, so rather than attempting to model the intricacies of the geometry, we elected to model the optimum mix of HDPE and cadmium, and to compare the results to the previous design which was borated low specific gravity polyethylene. The general geometry was a simple sphere and is shown below in Figure 5. A similar

geometry was set up for the comparison to the borated low specific gravity polyethylene shield that was used previously for the DARHT accelerator target chamber shield.

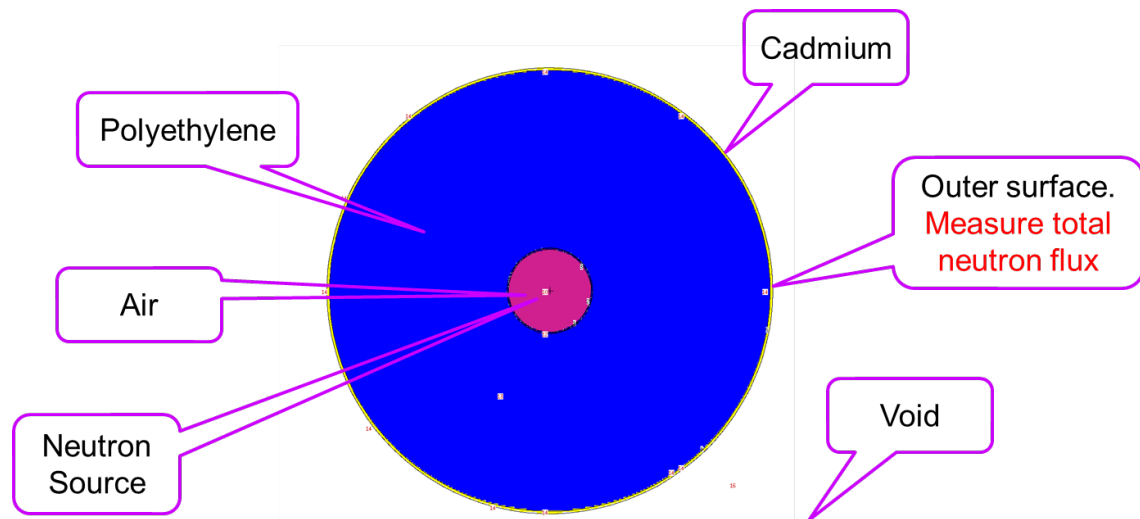


Figure 5: MCNP Output plot showing basic evaluation geometry of a simple sphere. The neutron source is at the center. The shielding consists of varying thicknesses of HDPE and cadmium, or conversely, of borated low specific gravity polyethylene.

The results for these MCNP studies are shown below in Figure 6. These calculations show that the new design using HDPE followed by cadmium is considerably more effective at neutron attenuation than the previous design using the low specific gravity borated polyethylene. The benefit becomes more pronounced as the shield becomes thicker. The target shield, because of its specific design, has many effective thicknesses. However, for all cases the new design has better attenuation.

There is one other mitigating factor for this shield. The front of the target shield must remain open, so as not to attenuate or scatter the X-ray flux from the accelerators. Therefore, a significant portion of the generated photo neutron flux will exit this aperture and will not be attenuated. Moreover, the photo neutron production process will focus the neutron flux in the forward beam direction, so that there still will be a neutron flux.

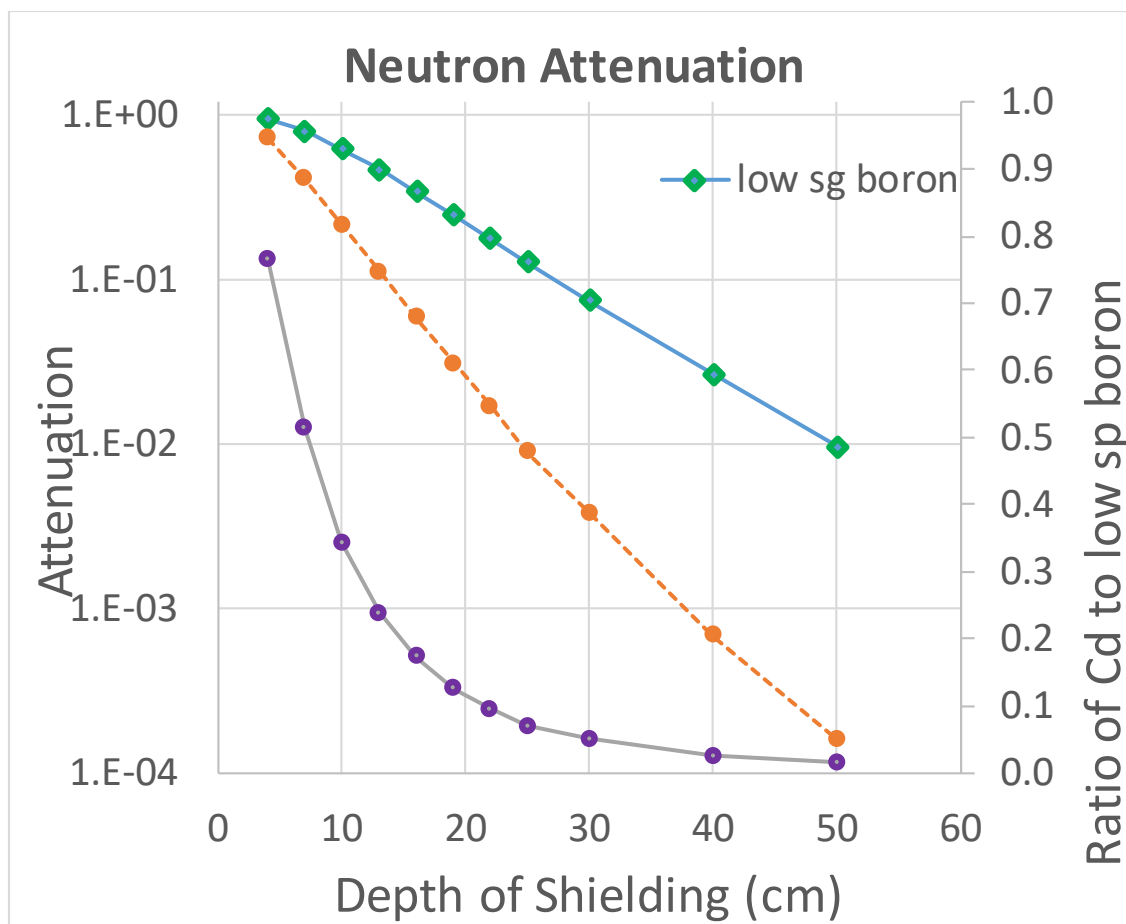


Figure 6: Results of the MCNP study showing the neutron attenuation as a function of the depth of the HDPE shielding (and assuming a fixed thickness for the cadmium sheet on the outside of 0.100"). The attenuation effect of the low specific gravity borated polyethylene is also shown. Finally the ratio between the two is plotted. The HDPE + cadmium performs significantly better at all thicknesses, but the improvement is greater for larger thicknesses, as the ratio plot shows.

2. GRC Shielding Conceptual Design

We also conducted an MCNP study of a notional shield design. Again, the intent was not to model the entire geometry and predict future performance. Rather, the intent was to explore the “sandwich” design, as is shown in Figure 4 above, and determine the optimum thicknesses for the various materials. The MCNP calculation can capture all the physics discussed in sections II.A and II.B above, with a particular emphasis on the coupled problem that neutrons create gamma rays by neutron absorption and gamma rays create neutrons by the photo-neutron process. We chose as materials lead for gamma-ray shielding and cadmium for neutron absorption. However, in our actual implemented designs these materials were replaced by steel and boron respectively because of the toxicity of lead and cadmium. However, the principles remain unchanged, the sandwich design remains unchanged, and the thicknesses only changed modestly.

In order to test just the relative thicknesses of the sandwich-design materials, we used the simplest geometry possible: a sphere. This approach is identical to that used in section II.C.1 above for the target chamber shield. The general design for this test shield is plotted below in Figure 7. The various material types are annotated and the MCNP calculation is run for multiple variations of the material thicknesses.

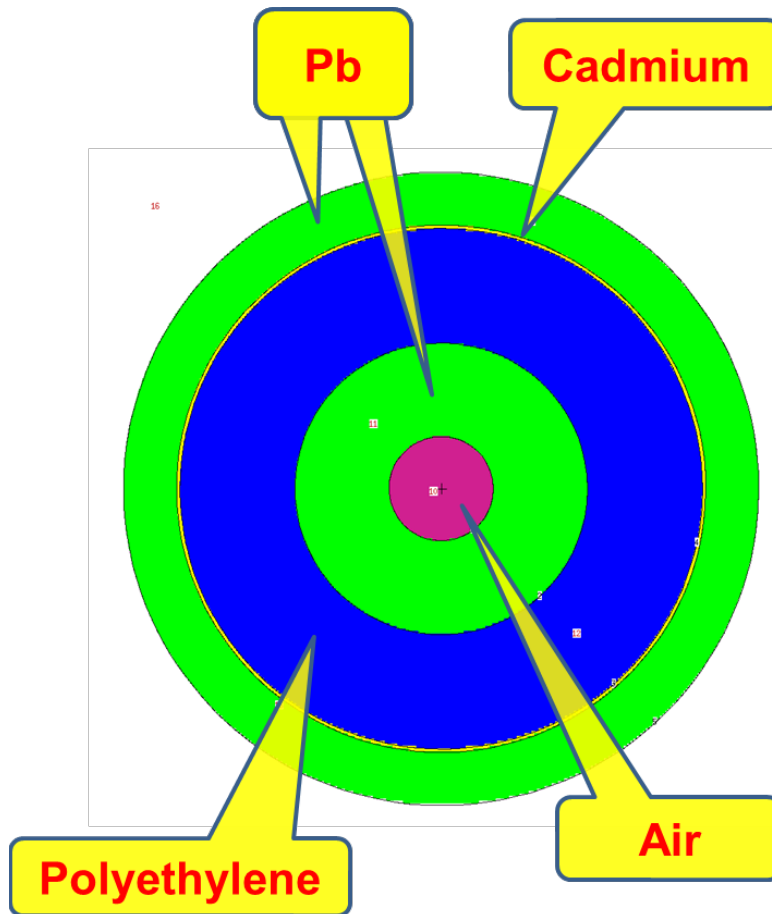


Figure 7: MCNP output plot showing the general design of a spherical "sandwich" design to evaluate shielding. The MCNP tests vary the relative thicknesses of each of the layers to optimize the shielding (minimize the amount of neutron and gamma radiation that makes it through the assembly). The various material types are annotated. The radiation source is at the center.

Dozens of different scaling runs were performed, which would vary one parameter at a time. Then, using the optimum parameter for one run, another series of MCNP calculations would be run that would vary a different parameter. Slowly, an optimal point was found that provided the best shielding for a constrained total thickness and for these material types. Total thickness was constrained for the obvious practical reasons. Although these tests were done using lead and cadmium, similar results are obtained for steel and boron.

A critical consideration when performing these calculations is to consider also the relative incident fluxes of neutron and gamma rays. As the gamma-ray flux is much larger, it is the more critical parameter.

Figure 8 below plots one set of MCNP data. The exiting gamma and neutron fluxes are plotted against the thickness of the initial lead layer. Note, that as this layer becomes thicker, the next layer, made of HDPE must become thinner to preserve the total thickness of the shield. We chose a total thickness of 13 inches in order to save space in the constrained Weather Enclosure. The plot normalizes the exit fluxes to those from a concrete slab that is nearly twice as thick at 24 inches.

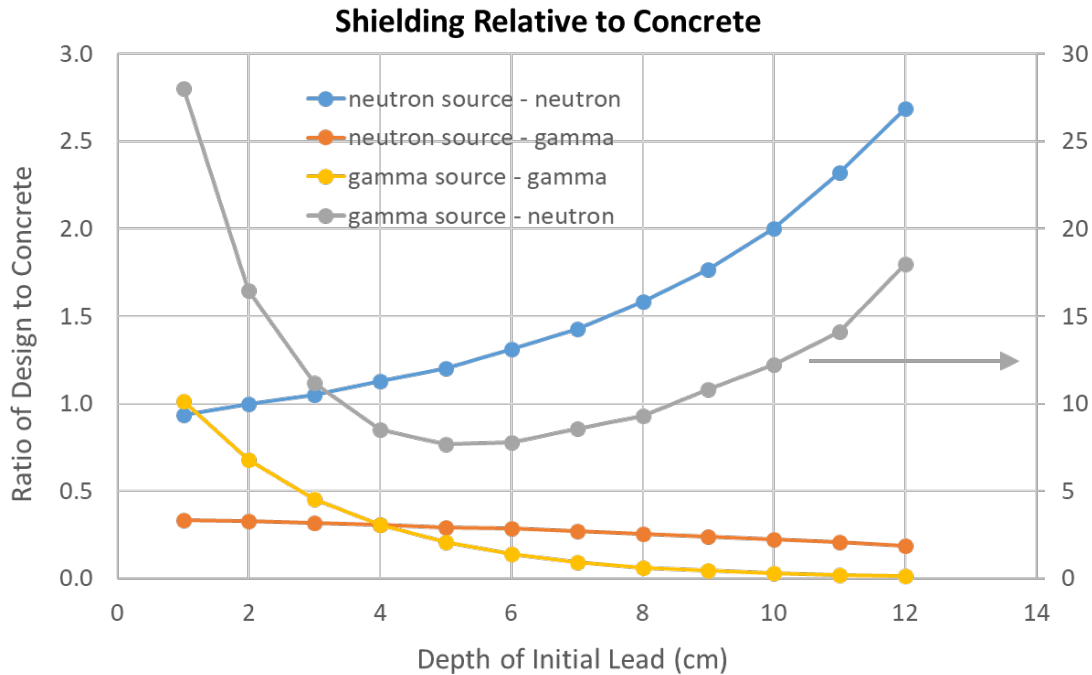


Figure 8: Plot of both neutron and gamma-ray transmission as a function of initial lead thickness in cm. The resulting data are also plotted for the source particle. Also, the total thickness of this shield is only 13 inches, but it is compared to a concrete block that is 24 inches thick. The reason is that we were attempting to make the shielding smaller, because of space constraints in the Weather Enclosure

III. Design of the Steel and Polyethylene Shield Walls, Shine Shield, and Concrete Walls

Figure 9 below is a schematic representation of the DARHT firing point layout of the top view looking down. The major components are the GRC enclosures, the two accelerators, the concrete shielding, the confinement vessel, and the steel-poly wall enclosure. These are annotated. The shielding design wraps around 3 of the 4 sides of both GRC houses, because the shielding must protect against radiation from both accelerators. The steel-poly wall also has a top shield (not shown), called the shine shield, to protect against radiation that scatters from the air above. (As discussed above in section II.B, this is mostly gamma-ray flux that has been Compton scattered).

The concrete blocks are quite large and heavy, but they have the singular advantage that they are blocks. So, the individual blocks can be moved and restacked relatively easily, as compared to a structure, such as the steel-poly wall, for example. So, although we found that a carefully designed shield using steel, HDPE, and cadmium could provide a more effective shield for a fixed depth, we chose to continue with the concrete blocks.

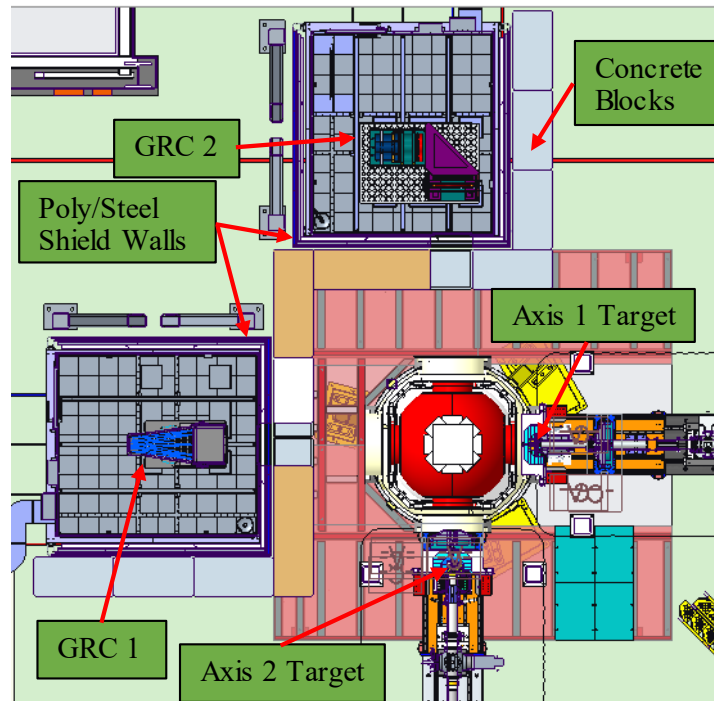


Figure 9: Pictorial of the DARHT firing point and the new Weather Enclosure. Annotations show the GRC houses, the accelerator target chambers, the concrete walls, and the steel/ poly wall. The shine shields are on top of the GRC houses.

A cross section view showing the design of the steel-poly wall is shown below in Figure 10. As can be seen, the general design follows the discussion from above: the sequence of materials is steel, HDPE, borated polyethylene, a boron sheet, and more steel. Boron was selected rather than cadmium because of its toxicity. The initial steel layer is intended to shield the modest energy, Compton scattered, gamma rays to prevent photo-neutron production in the final layers. Subsequent layers attenuate the neutron flux using HDPE, borated polyethylene, and boron. The final steel layer shields against gamma rays from all sources.

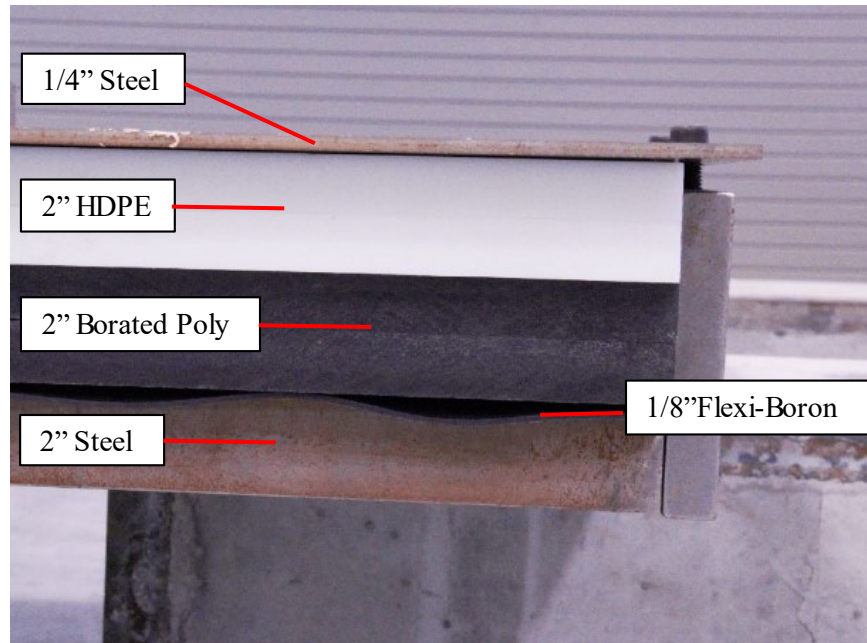


Figure 10: Basic design of the steel / poly wall shown in cross section. The basic design follows the description in the text: steel followed by HDPE, then borated polyethylene, Flexi-Boron, and steel.

The final shield assembly is shown below in Figure 11 from the back, looking in toward the firing point. The new (lighter) GRC enclosures are moved inside of this shield enclosure and are aligned. The essential features are the concrete blocks on the outside, the poly-steel wall on the sides, and the shine shield on top, which, recall, is just a steel gamma-ray shield. We emphasize that the modular design of the shielding allows for moving and re-aligning of the gamma-ray cameras. We also wish to note that the overall design has several elements and each is designed to shield against a particular interfering radiation. The GRC enclosures themselves shield against visible light (which would directly interfere with the cameras), and EMI (which interferes with the electronics). The concrete and steel-poly wall shield against both neutrons and gamma rays. The shine shield (steel-poly wall ceiling), shields against gamma rays.



Figure 11: Picture of the built and installed steel / poly wall with shine shield on top and Borated concrete blocks surrounding.

In addition to this primary shielding, we also developed the port collimator shields. Those will be discussed in section IV below. We also built and installed an improved neutron shield around the target chambers of both accelerators. The design was discussed in Section II.C.1 above.

IV. Design of the Port Collimator Shields

The port collimator shields were designed, built, and installed because there was a large aperture in the GRC enclosure, the concrete wall, and the steel-poly wall. The dimensions of the apertures in the concrete and the steel-poly wall matched closely the aperture size of the GRC enclosure. Scattered gamma rays and photo-neutrons are concentrated along the direct X-ray beam. Therefore, most of the scattered radiation will occur along the periphery of the beam line itself. To mitigate this effect, the port collimators, were designed to reduce the acceptance of the X-ray beam to just slightly larger than the direct X-ray beam. This shield was developed after we had already begun testing; we had found out in our initial measurements that significant flux was entering the GRC along the beam line periphery. The port collimators were added to mitigate the neutron and gamma flux in the beam line periphery. The port collimators closely match the original design of the GRC blast houses and hence provide similar collimation.

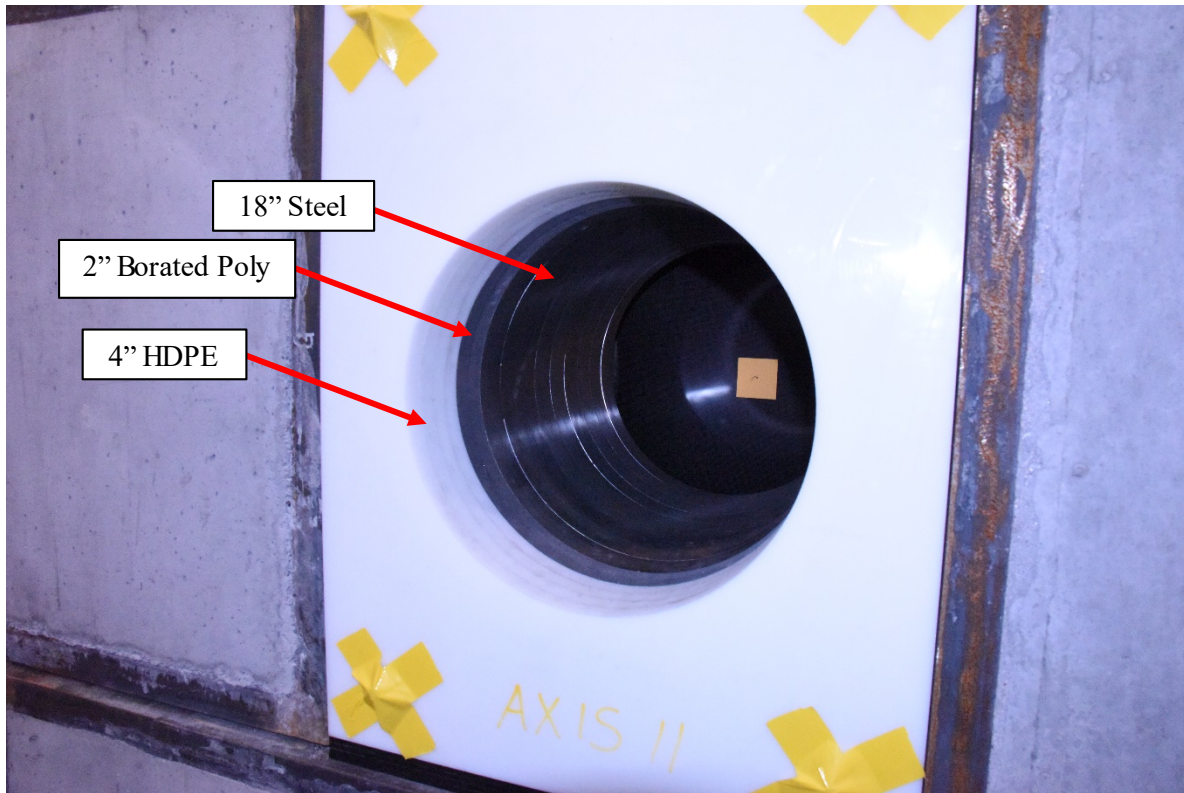


Figure 12: Picture of a complete port collimator installed upstream of the Axis 2 GRC enclosure. Note that four inches of high density polyethylene and two inches of borated polyethylene are located just upstream of the steel.

Figure 12 shows the completed and installed port collimator for Axis 2. The design follows the same approach as discussed previously: HDPE, borated polyethylene, and steel. As is immediately apparent from this figure, the effect of the port collimator is to collimate the total radiation beam to just that needed to accept the direct X-ray beam. The layered design and modest size of the port collimator allows be mobility; similar to one of the blocks of concrete. As such the port collimators can be moved independently using the WE overhead crane. Thus, we can disassemble the port collimator and concrete wall block by block. This capability allows us to reconfigure the firing point, which was one of the original requirements.

Figure 13 below shows the layered design of the steel component of the port collimator. The layered design was selected principally for ease of mechanical fabrication and machining and matches the design of the original GRC blast house ports. Individual plates were machined and then welded together. Steel shims were used to align the port collimators to the X-ray beams. Lastly, the HDPE, and borated poly sheets are bolted to the steel port collimator assembly.

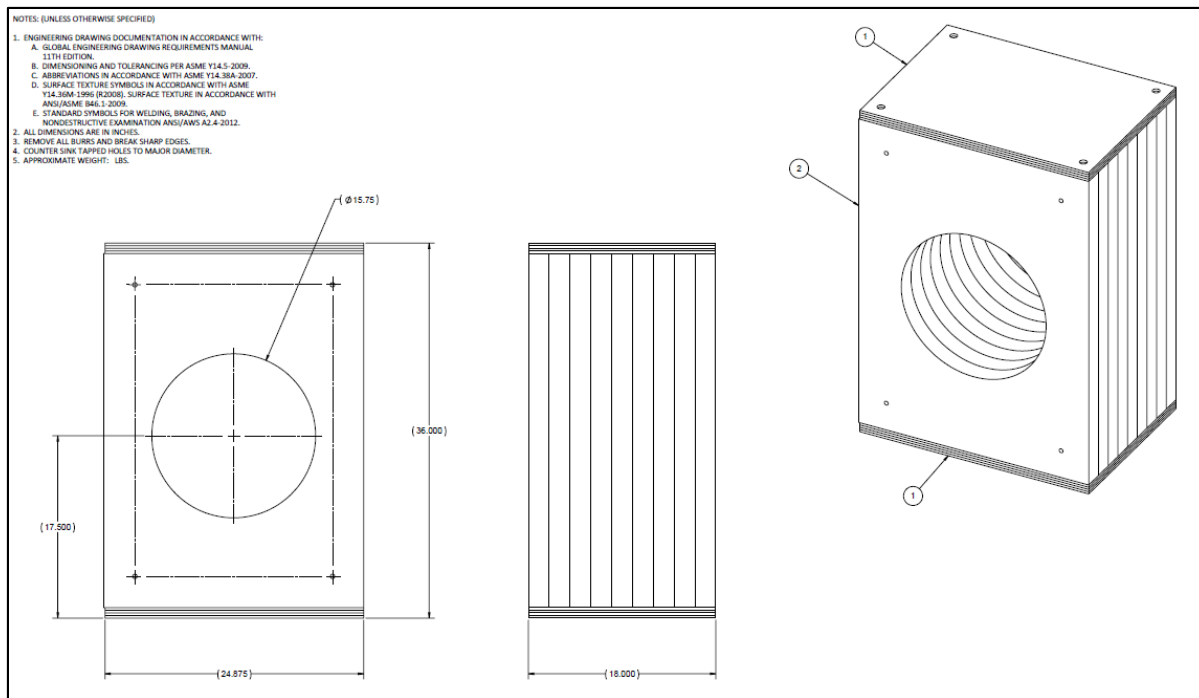


Figure 13: Design of the steel portion of the port collimator shields.

V. Experimental Approach and Measurements

There have been two goals to this shielding study: first,

- To provide the highest image quality for DARHT radiography, and
- To understand the interference mechanisms and how to best mitigate them.

Therefore, we installed different stages of shielding separately, so that we could make measurements for each particular case. That way we could correlate the improvements in radiation interference with particular shielding configurations. The results reported in this report will be organized around each of the individual shielding configurations, going from least to most. These are: just concrete walls, concrete walls and the steel-poly wall with the shine shield, and finally with the addition of the port collimators. All cases included the new target region shield.

We also used multiple instruments to measure the radiation, in order to further identify the sources and pathways. These measurements included:

- Neutron bubble detectors, which measure the neutron dose over a broad range of energies.
- Neutron “pulsed” detector which measure the integrated neutron dose for just a short period of time for a broad range of energies.
- Phosphor packs. These are passive gamma-ray detectors that we still use as a backup imaging device in the event that the gamma-ray cameras fail during a shot. They are sensitive to the gamma-ray flux in the energies typically produced by the DARHT accelerators. They record an image, so that differences in the gamma flux are apparent.

- The actual gamma-ray cameras themselves. Indeed, the whole point of the shielding is to minimize the radiation interference to the cameras. Therefore, the interference signal on the cameras turns out to be the most informative of the overall radiation signature.

We found that of all the gamma-ray and neutron measurement systems that we could find, that the most effective and sensitive measurement of neutron and gamma-ray interference was the GRC cameras themselves. So, as we proceed through this report, we will show the reduction in radiographic interference as each of the components of the entire shielding system was installed.

Another effective measurement was the phosphor imaging plates. These were strategically positioned to measure x-ray flux in locations of interest. This allowed us to create a simple map of x-ray intensity that showed where the major shielding gaps were located. Surprisingly, we found that there is a significant Compton scattering component from just air, so that the gamma-ray field was also broadly distributed. But, using the phosphor packs we learned where shielding was important. (The short answer is everywhere).

Neutron bubble detectors were used inside and outside of the shielding to obtain similar map for neutrons. The bubble detectors are also calibrated to neutron energy and dose and therefore can provide actual dose information at various locations. Lastly a pulsed neutron detector, Albatross 2080B, was used to provide an additional neutron dose diagnostics for cross comparisons with the bubble detectors. The neutron bubble detectors were used with just the concrete wall. The intent was to determine the neutron field throughout the firing point area. Not surprisingly, the neutron field is strongest outside the shielding. The locations of the neutron bubble detectors on the firing point is shown Figure 14 below.

Finally, the design of the shielding was informed by the basic theoretical considerations and the MCNP studies discussed in II above.

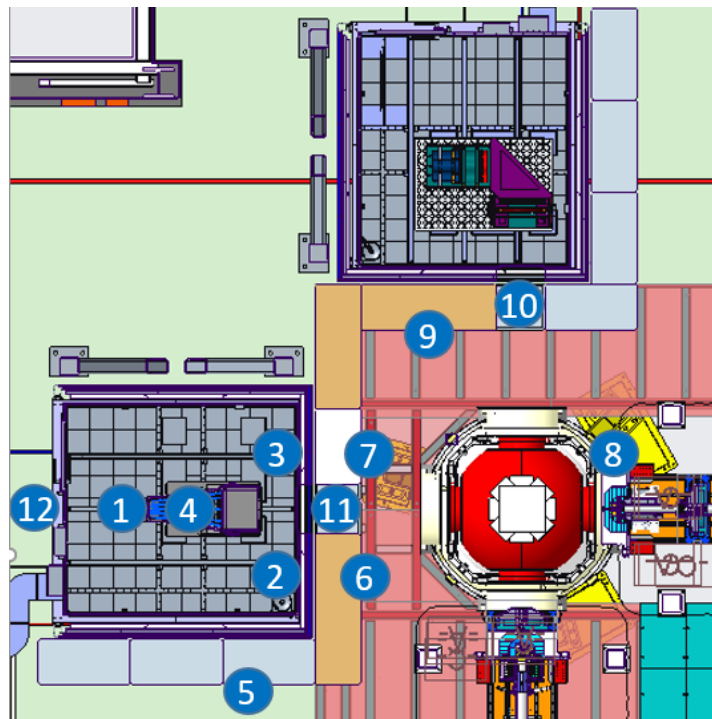


Figure 14: Layout showing the positions of the neutron bubble detectors.

The positions of the Albatross 2080B pulsed neutron detectors are shown in Figure 15 below. These were intended to determine the specific neutron field both inside and outside the GRC enclosures.

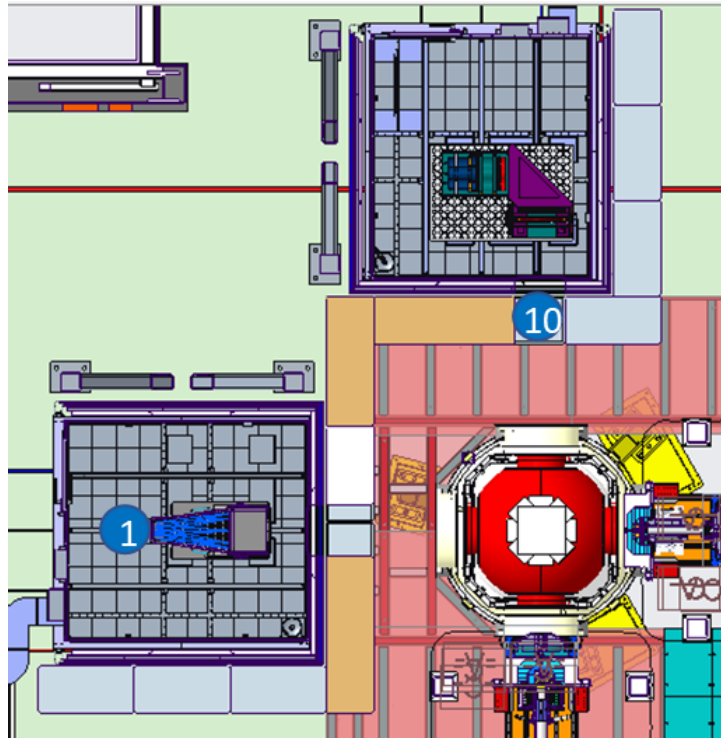


Figure 15: Layout showing the positions of the Albatross 2080B pulsed neutron detector.

VI. Results with Just Concrete Walls

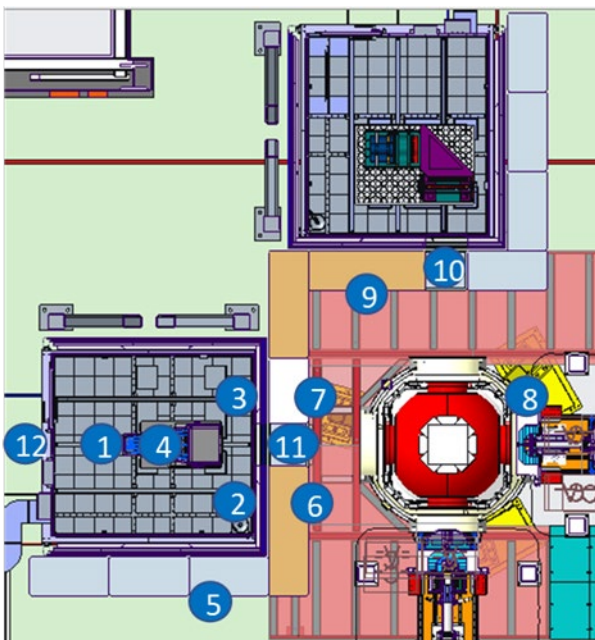
The first set of measurements were done with just the concrete walls. These measurements provided the baseline for the subsequent additional shielding installations. The reason that the concrete blocks were used initially (rather than no shielding) was to protect the sensitive gamma ray camera detectors and electronics. The large neutron (and primarily gamma) fluxes would damage this electronics without some level of shielding.

The measurements with the concrete walls included all of the radiation diagnostics discussed above: neutron bubble detectors, neutron pulsed detectors, phosphor packs, and the gamma-ray cameras. The reason that the neutron bubble detectors, and phosphor packs were used only with the concrete walls is that we wanted the largest possible fluxes so that the signals would be large and the measurement precision, (counting statistics), will be as good as possible. The phosphor packs are used only to identify the significant pathways for the interfering radiation. Each of these measurements will be discussed in the sections below.

A. Neutron Bubble Measurements Results

Figure 16 below shows the neutron bubble detector measurements taken at the locations shown. The bubbles are counted in a special detector and converted to the integrated value of the neutron field with units of millirem (mrem). These values are normalized to the number of identical Axis 1 accelerator pulses (focused, mode 2). These results are not surprising: the neutron field is much larger outside of the concrete walls. It is larger in line with the main gamma-ray beam. However, somewhat surprisingly, very little seems to get inside the GRC enclosure itself, indicating good neutron shielding performance of the borated concrete blocks. Also, there is considerable scattering of the neutrons, so that large values were seen

perpendicular to the gamma-ray beam (detector location 10). Indeed, detector location 11 was inline, but outside the concrete and showed a lower value than detector location 10, suggesting, perhaps a $\frac{1}{R^2}$ scaling.

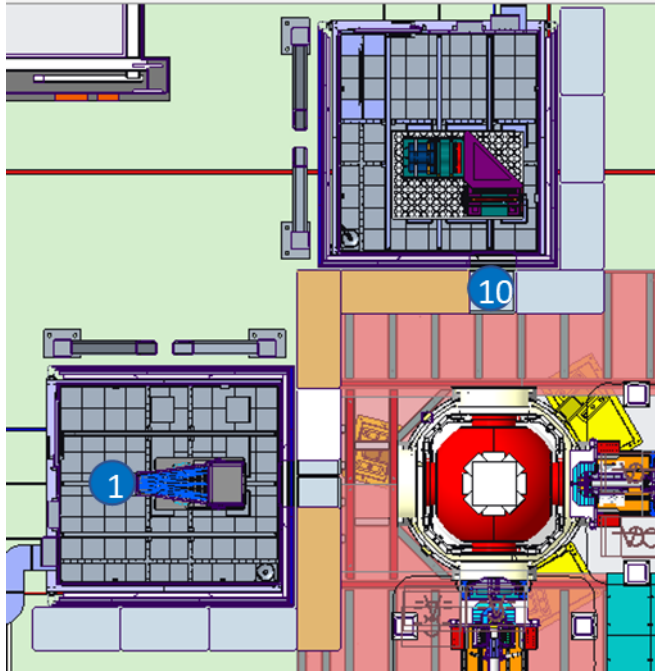


| Detector Location | Dose (mrem) |
|-------------------|-------------|
| 1 | 0.09 |
| 2 | 0.06 |
| 3 | 0.05 |
| 4 | 0.09 |
| 5 | 0.06 |
| 6 | 2.3 |
| 7 | 2.3 |
| 8 | 7.1 |
| 9 | 3.4 |
| 10 | 2.2 |
| 11 | 1.1 |
| 12 | 0.06 |

Figure 16: Neutron bubble detector results. The values shown at each position (left) are normalized to the number of pulses from the Axis 1 accelerator and are shown in the table (right) in mrem/pulse.

B. Pulsed Neutron Detector Results (Albatross 2080B)

The pulsed neutron detector results are shown below in Figure 17. These measurements are again converted to units of millirem and correspond to an individual shot from Axis 1. In this case the results are shown at position #1 for all three shielding cases: concrete only, concrete with poly-steel wall, and all shielding installed. Position #10 is outside the concrete shielding and is shown for reference. The results are largely as expected. The poly-steel wall reduced the neutron flux by a factor of about 1.6. However, the port collimators reduced the neutron flux by another factor of 3. This result provides exactly the information we needed: the dominant pathway for the neutron radiation is along the beamline. Fortunately, the neutrons can pass right through the scintillator, the visible light turning mirror, and can exit the GRC enclosure. It is also somewhat beneficial that the GRC enclosure is much less thick than the predecessor, so that the neutrons can exit relatively easily.



| Shielding | Detector Location | Dose (mrem) |
|----------------------------|-------------------|-------------|
| Concrete Only | 1 | 0.05 |
| +Poly/Steel & Shine Shield | 1 | 0.03 |
| +Port Collimators | 1 | 0.01 |
| Reference | 10 | 6.3 |

Figure 17: Pulsed neutron detector results. The values shown at each position (left) are normalized to the number of pulses from the Axis 1 accelerator and are shown in the table (right) in mrem/pulse.

C. Internal to GRC Enclosures Measurement Results

The phosphor packs were also used with the concrete shielding only. Their purpose was explicitly to determine the pathways for the interfering gamma-ray radiation. It was not to determine the absolute, calibrated gamma-ray flux. The phosphor packs show a lighter color when exposed to larger gamma-ray fluxes. They are insensitive to visible light, so that they can be positioned in advance (just as we do for a real hydrotest). The images are read by a scanner, specifically designed for this purpose. The images provide a very nice picture of where the gamma flux is entering the GRC enclosure.

Figure 18 below shows the result from the first phosphor pack. It was installed on the ceiling of the GRC, so it measured the gamma-ray flux entering the top of the enclosure. As these conditions only had the concrete wall in place, there was no shine shield installed. This flux is directly the result of Compton scattering of high energy gamma-ray photons from the air and surrounding materials. It is likely that the source of photons was the penumbra of the gamma-ray beam.

The image on the left of Figure 18 shows the location; (it is a picture looking up). The image on the right is the scanned phosphor pack image. It is clear that under these circumstances, the gamma-ray flux from the Compton scattered photons is largely uniform across the unshielded ceiling of the GRC.

Figure 19 below shows a similar configuration: a second phosphor pack positioned on the front wall (facing the accelerator) of the GRC house but overlapping with the aperture in the concrete and GRC enclosure. Again, the picture on the right shows the position of the pack, and the picture on the right shows the results.

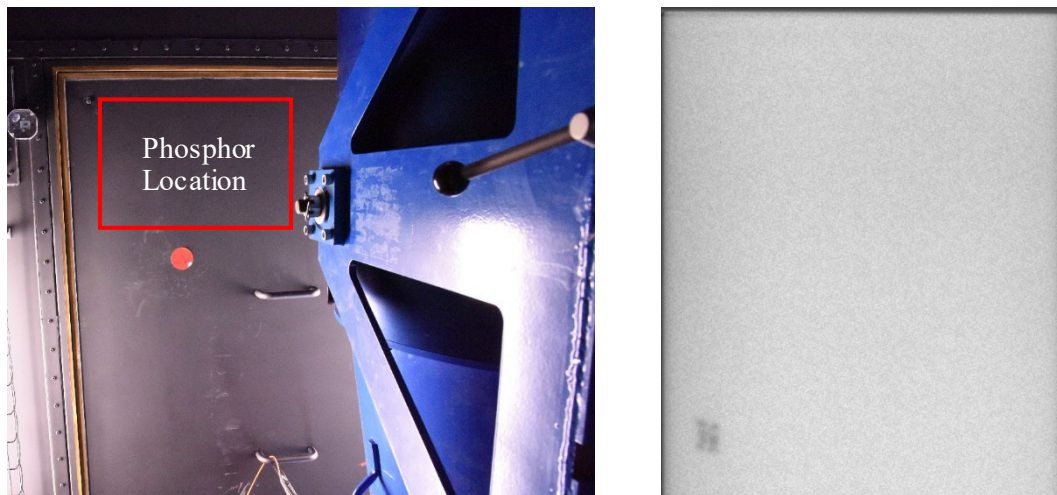


Figure 18: Phosphor image plate location (left) used in measurement of gamma-ray flux flowing through the ceiling of the GRC enclosure. The picture is taken looking up from the optics table. The image from the plate (right) shows an evenly distributed intensity which implies that x-rays are entering somewhat uniformly over the entire ceiling.

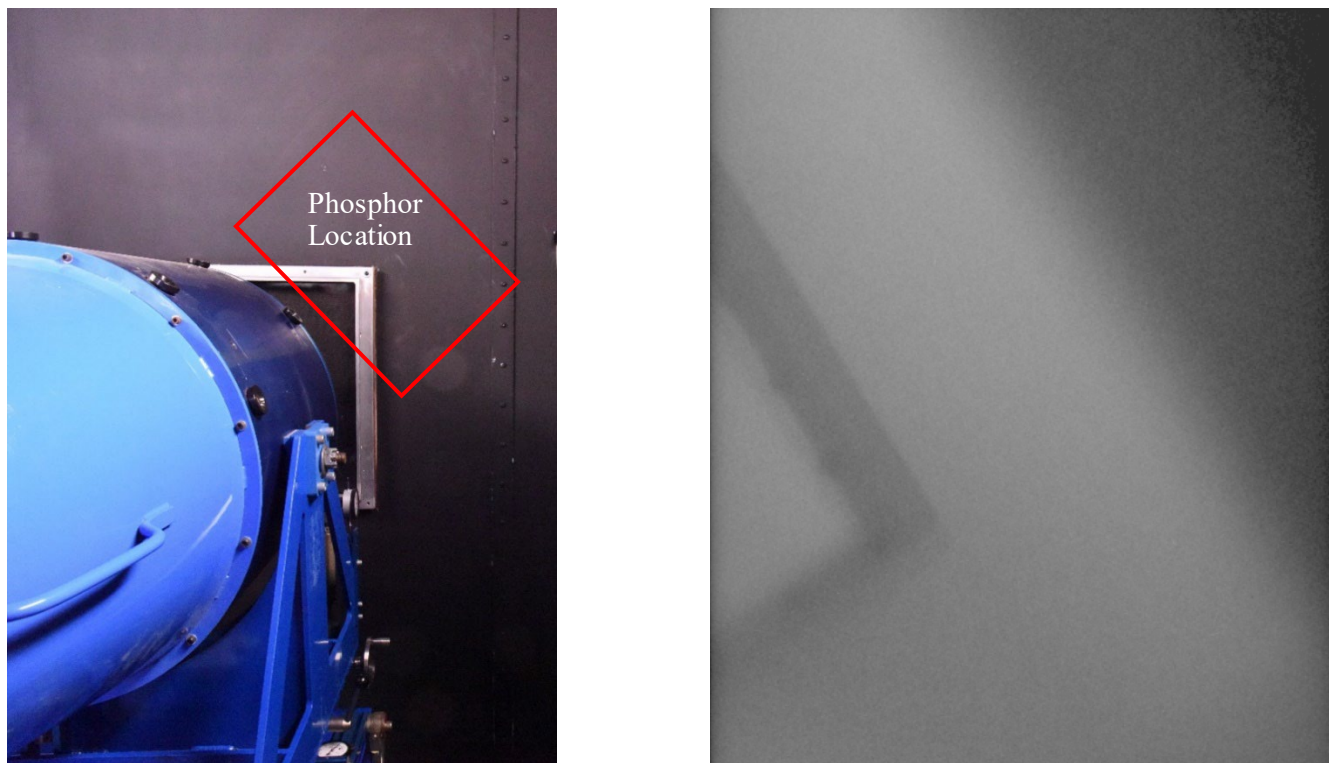


Figure 19: Phosphor pack measurement of gamma-ray flux flowing through the front wall of the GRC enclosure. Note the increased flux at the edge of the rectangular opening, lighter areas are higher flux, darker areas are lower flux.

The results from Figure 19 show that the gamma-ray flux that penetrates the concrete is significantly lower compared to the fully unshielded flux that enters through the GRC enclosure and concrete wall aperture.

The aperture of the concrete wall is clearly shown in the image, illustrating the need d for additional shielding and collimation of the scattered X-ray beam. Without further collimation and shielding of this scatter, a significant photon and neutron flux enters the camera enclosure. We conclude, that just as with the neutron flux, that implementing the port collimators is an essential addition to the overall shielding design. Indeed, these results were obtained before the port collimators were designed and built, and were the experimental motivation for that addition.

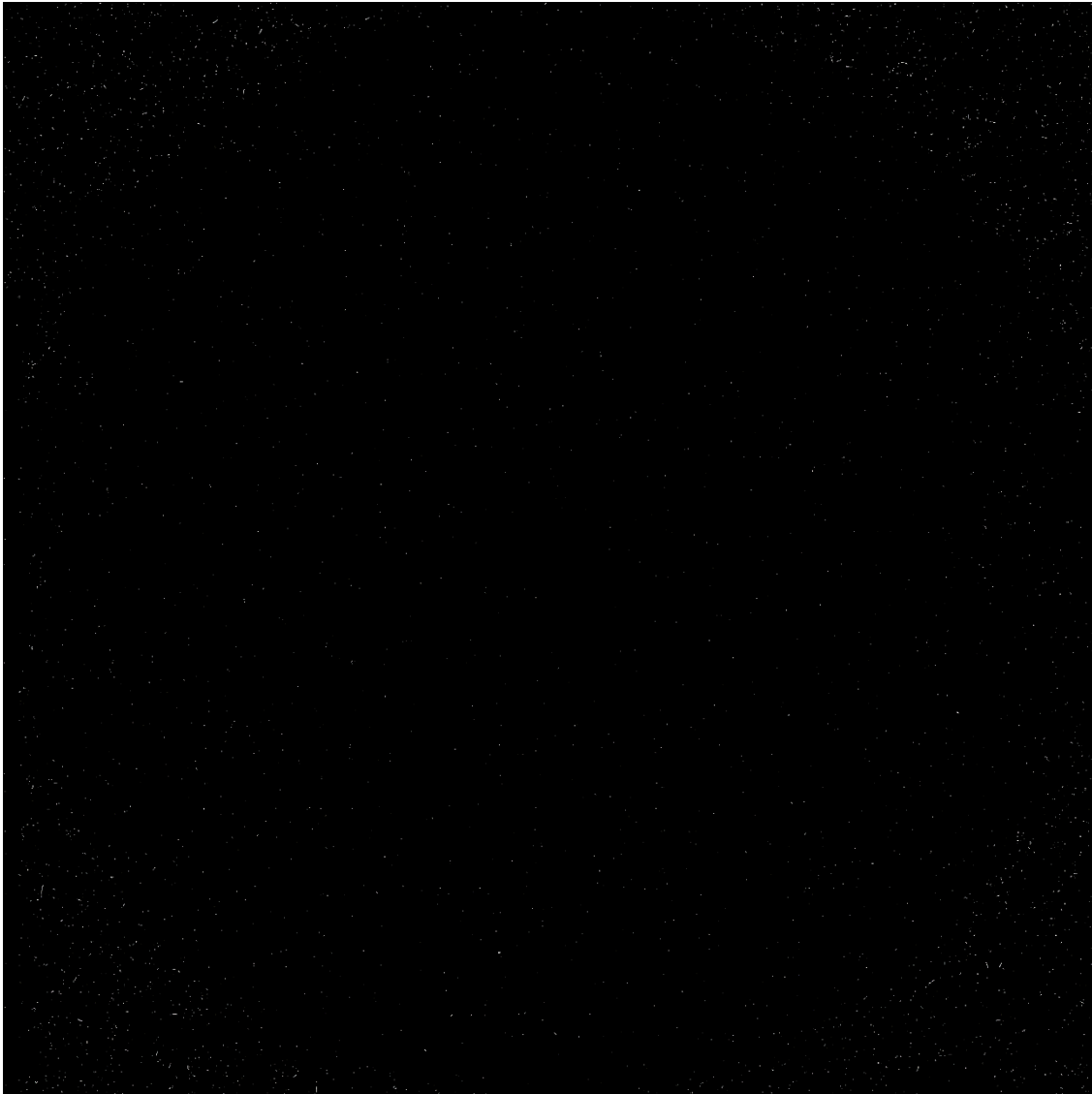


Figure 20: Gamma ray camera image showing star events as a result of direct particle interactions with the CCD with concrete blocks as shielding only. This image was generated using the L. A. Cosmic algorithm on a Flat Field image. In this case, 8,335 star events were recorded. Note the presence of tracking in the image which is indicative of charged particle interactions in the CCD. The accelerator dose in this image was 405 rad @ 1 meter.

Arguably, the most important measurement is the one made by the gamma-ray cameras themselves, as the interference is the issue we are attempting to solve. Moreover, by using the L. A. Cosmic algorithm [6] we can count the number of interference “stars” that appear in the flat field image and strictly quantify the level of radiographic interference that comes from the adverse neutron, gamma, and other radiation fields. Figure

20 above shows the flat field image for the case of just concrete shielding. Although the “stars” may be difficult to see, the software has extracted their number as 8,335 star events with an accelerator dose of 405 rad @ 1 meter. This provides our baseline for improvement of the overall shielding design.

VII. Results with Steel and Polyethylene Walls and Shine Shields Installed

The next step in our experiments was to measure the radiation fields and their effects on the camera images with the concrete, the steel-poly wall, and the shine shield installed. It should be noted that this case does not include the port collimators. We measured the internal neutron field for this case, and these results were presented in Figure 17 above. Moreover, the shine shield (recall, this is the ceiling on the steel-poly wall), should specifically address the gamma-ray flux through the GRC ceiling, as was shown in Figure 18 above. However, arguably the most important measurement was the actual interference suffered by the gamma-ray camera. The gamma-ray flat field image for this case is shown in Figure 21 below. The improvement is significant. The quantification of the residual interference is the number of “stars” counted by the L. A. Cosmic algorithm from this image is 4,958 at an accelerator dose of 393 rad @ 1 meter. The results clearly demonstrate the improvement of the overall steel-poly and shine shield design. However, our previous results showed that a significant amount of adverse radiation enters through the shielding aperture, which is addressed in the next section.

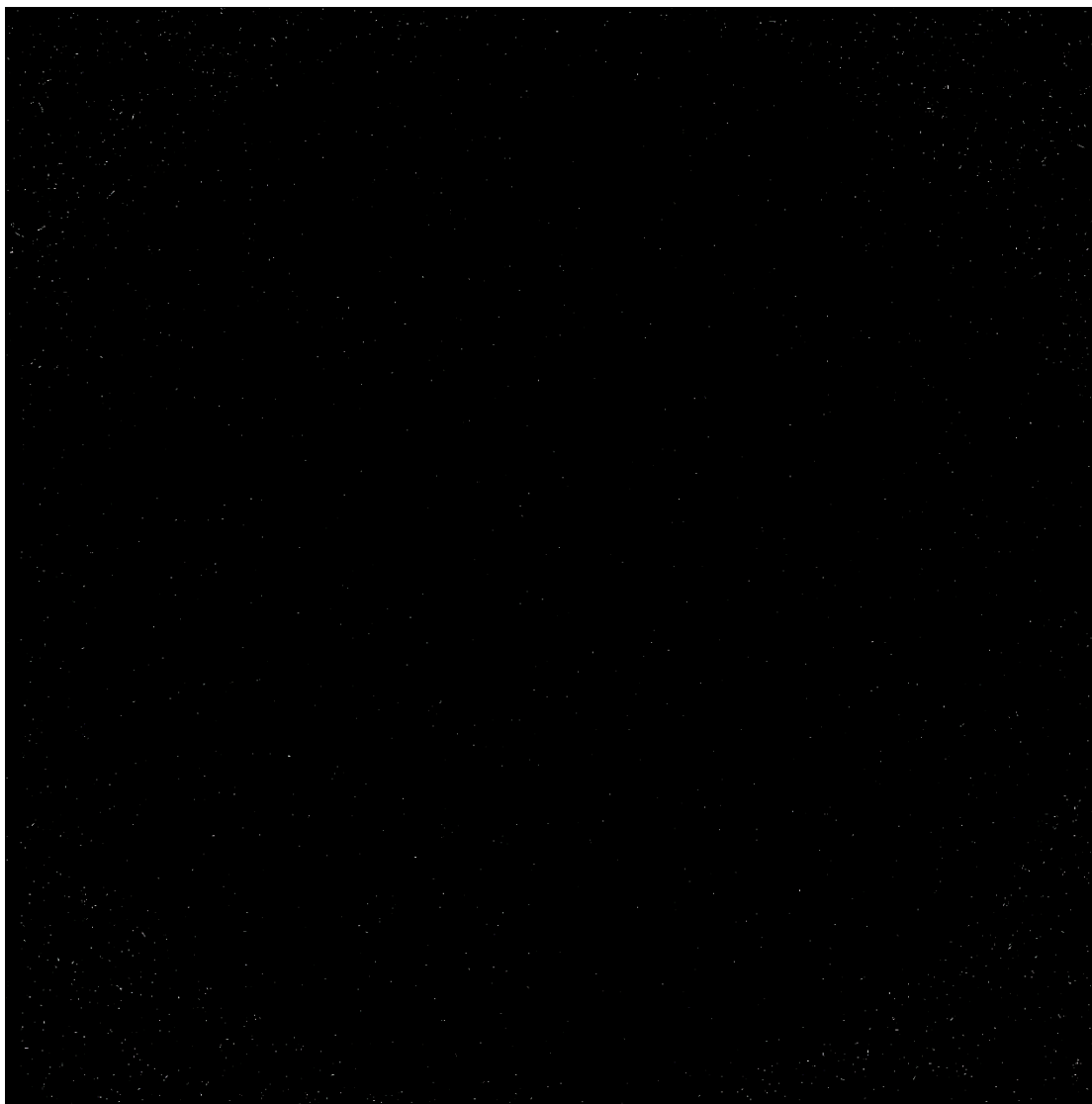


Figure 21: Gamma ray camera image showing star events as a result of direct particle interactions with the CCD with concrete blocks, poly steel walls and steel shine shield. This image was generated using the L. A. Cosmic algorithm on a Flat Field image. In this case, 4,958 star events were recorded. In addition to the overall reduction in events, note the reduction of tracking in the image as compared to Figure 19 (Concrete Blocks Only). The accelerator dose in this image was 393 rad @ 1 meter.

VIII. Results with All Shielding Installed Including Port Collimators

The final measurement of interference with the radiographic image is shown below in Figure 22. The total count from the L. A. Cosmic software is 5,168 which is nearly equivalent to the results in Figure 21. However, in this case the DARHT Axis 1 accelerator dose was nearly 25% higher at 520 rad @ 1 meter. This case consists of the full suite of shielding installed, which includes: the neutron shield of the target chamber, the wall of concrete blocks, the poly-steel wall, the shine shield, and the port collimators. The overall shielding performance with nearly a 25% increase in dose is significant. These are our final results for this experimental series. The results are also summarized in Table 1 below.

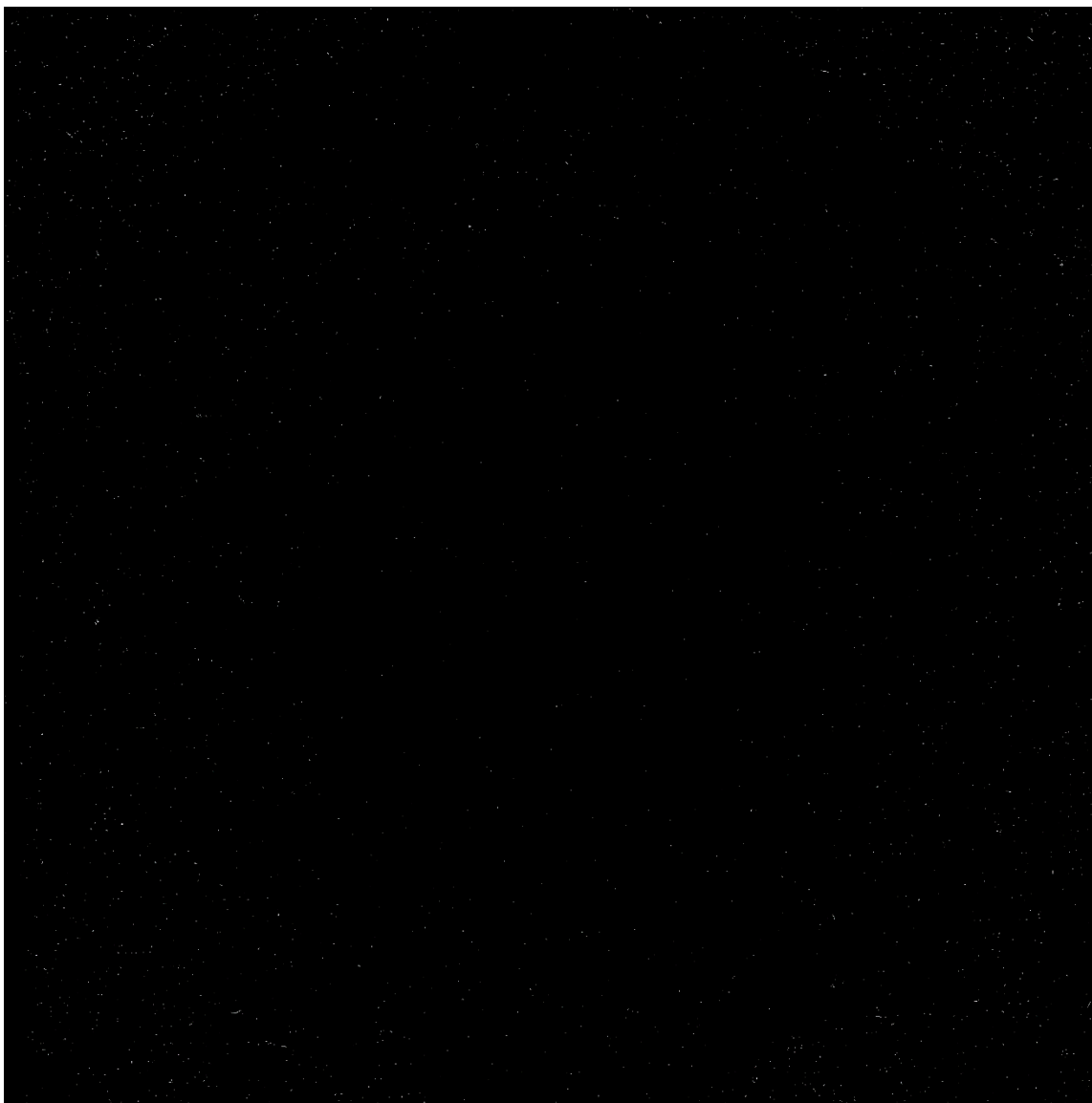


Figure 22: Gamma ray camera image showing star events as a result of direct particle interactions with the CCD with concrete blocks, poly steel walls, steel shine shield, and port collimators. This image was generated using the L. A. Cosmic algorithm on a Disk and Washer image. In this case, 5,168 star events were recorded, nearly identical to the case in Figure 20 (Concrete, Poly/Steel, and Steel Shine Shield), however the accelerator dose was nearly 25% higher at 520 rad @ 1 meter. The addition of the port collimators clearly enhanced the system shielding.

Table 1: Summary of counts of stars for shielding configuration.

| Case | Number of Stars | Accelerator Dose (rad) | Normalized Number of Stars |
|-------------------------------|-----------------|------------------------|----------------------------|
| Concrete only | 8,335 | 405 | 20.58 |
| + Steel-poly and shine shield | 4,958 | 393 | 12.62 |
| + Port collimators | 5,168 | 520 | 9.93 |

IX. BIE Analysis Comparison to Hydrotest 3682

There were many changes in the configuration of DARHT that were included under the auspices of the WE project. Perhaps the most significant was the re-design and rebuilding of the downstream transport sections of the two accelerators, to allow the VFoV capability. However, we wished to consider the full spectrum of radiographic image effects from all possible changes to the DARHT configuration in an effort to quantify the radiographic initial operating condition (RIOCI) following the Weather Enclosure project. In addition to quantitative measurements made above, we conducted a radiographic comparison of DARHT imagery before and after the Weather Enclosure using standard BIE image analysis procedures. Our approach was to tune the DARHT Axis 1 so that the accelerator performance and the radiographic targets were identical to a particular pre-Weather Enclosure case and perform an exhaustive survey of the two sets of radiographs.

We chose a standard gas cavity experiment, Hydrotest 3682, as our basis for comparison. The 3682 data was taken in the original DARHT firing point configuration prior to weather enclosure construction. An identical pre-shot radiography data set was taken in the new weather enclosure configuration replicating that taken prior to 3682. Both data sets used the Collimator Calibrator (CC) as the primary radiographic object. A side by side analysis was carried out using the standard DARHT radiographic analysis procedure. The resultant additive and multiplicative fields and forward model residuals were compared. The results showed that the data set taken in the new weather enclosure configuration, including all shielding and port collimators, are nearly identical to those taken in 3682. This implies that the modest increase in single pixel events compared to pre-weather enclosure data has a negligible effect on the standard BIE analysis results. This is mainly due to the image processing techniques that remove single pixel events from the data.

The following figures and discussion outline the complete radiographic comparison for before and after. Perhaps more significantly, any other changes that might potentially have affected the image quality appear to be negligible. A comparison of the processed radiographic images of CC object are shown in Figure 23. More quantitative analyses follow in subsequent images. A qualitative comparison of the CC radiographic images indicate that the overall DARHT radiography performance remains unchanged. The two images are visually identical.

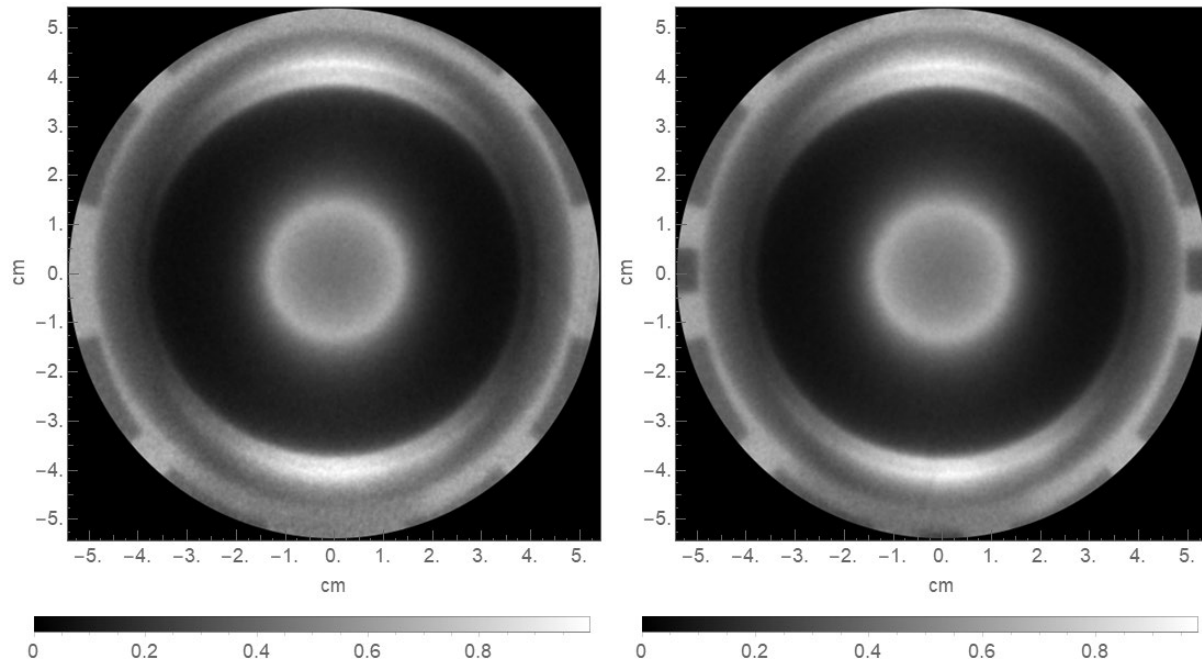


Figure 23: DARHT Axis 1 Radiographic images of the Collimator Calibrator object taken prior to hydrotest 3682 (left) and post weather enclosure (right).

However, to properly address a radiographic comparison, we must complete a quantitative analysis. The “by eye” comparison, is by contrast, strictly qualitative. The quantitative assessment is made possible by our image analysis software: the Bayesian Inference Engine (BIE) code. This code has been under development for decades, and is the standard software used for all DARHT radiographic analysis. A forward model of the radiographic data was created using the BIE. As inputs to the model, image metrics such as blur, noise, additive and multiplicative fields are fit to the radiographic data. Figure 24 shows the forward model additive fields for 3682 and post Weather Enclosure data as a function of radius for the CC object. Most importantly the two plots are nearly identical in shape indicating nearly identical radiographic performance. Small differences in magnitude of the additive fields are attributed to Hydrotest 3682 having a slightly larger beam dose than for the post Weather Enclosure case.

Figure 25 and Figure 26 below are variations on the same theme. A specific reduction of the image fields is performed and these are compared to the two measurement cases, before and after the Weather Enclosure. The fundamental difference between these and also Figure 24 are the normalization method of the Additive Fields. However, the essential issue is that these quantitative measures of the image can be directly compared between the images taken before the Weather Enclosure and the images taken after the Weather enclosure.

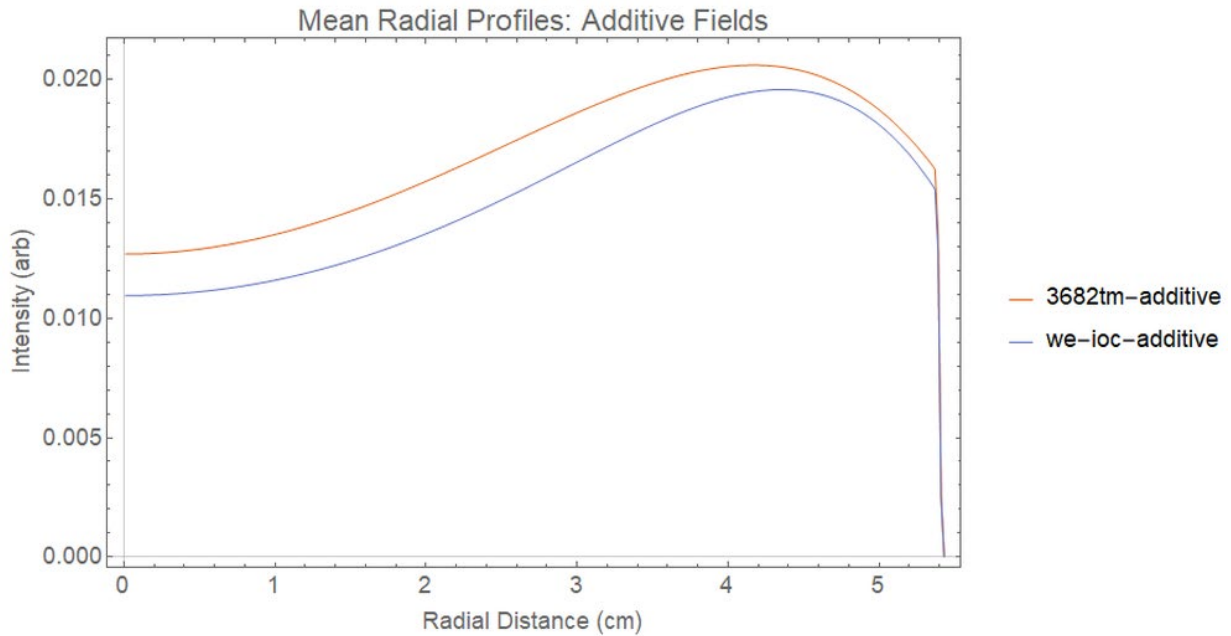


Figure 24: DARHT Axis 1 radial profiles of the Collimator Calibrator data for 3682 and post weather enclosure data. The similarities in field shape illustrate that the radiographic performance is very similar. The slight difference in intensity is due to a higher dose from the accelerators.

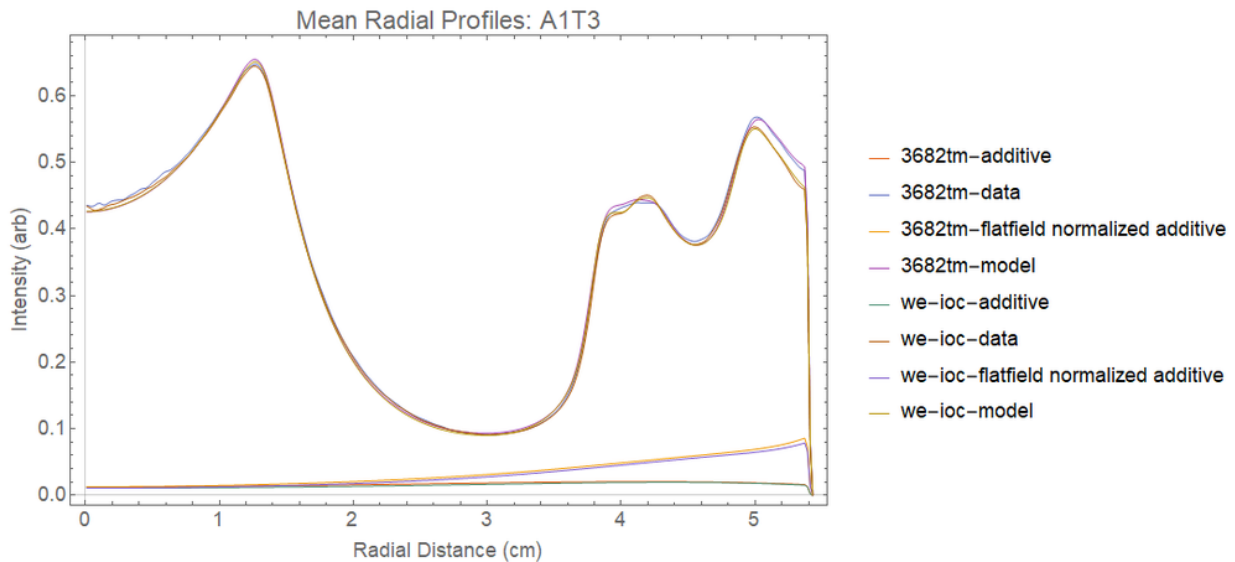


Figure 25: DARHT Axis 1 radial profiles of the Collimator Calibrator data, additive fields, and normalized additive fields for 3682 and post weather enclosure data. The distinct similarities in the shape the fields show that radiographic performance following construction of the weather enclosure is preserved.

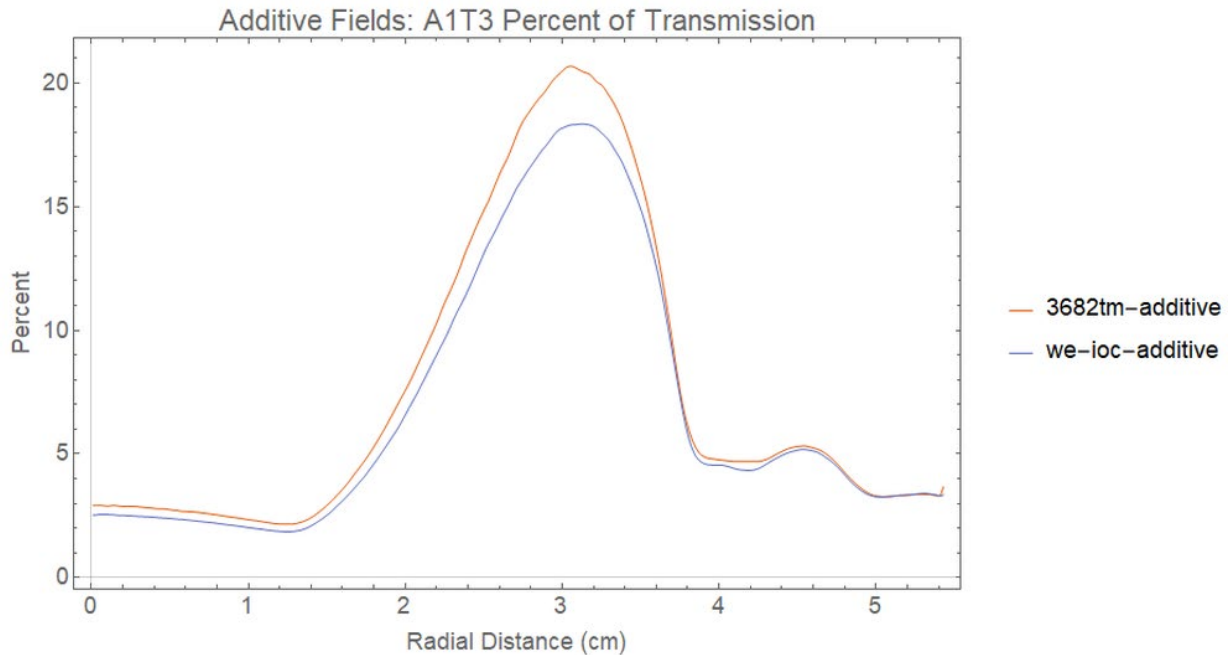


Figure 26: DARHT Axis 1 additive field radial profiles plotted as a function of percent of transmission. This plot shows less than a percent difference in most of the data when comparing the two data sets. The similar shape and relative similarities in percent of transmission indicate very similar radiographic performance.

Residual images of the CC forward model and data from 3682 and post Weather Enclosure are compared in Figure 27. The residual images are generated by subtracting the forward model radiograph and the data radiograph. The result is a quantitative measure of how well the forward model fits the data. The forward model includes the actual object dimensions and material, and the performance of the entire DARHT radiographic chain from accelerators through the GRC. All of the system operation is well-known and characterized, so it is possible to work the problem in the forward direction and take a known object and calculate the image that it should produce in DARHT. The issue here, however, is not that the residual exists, but that the residual map is nearly identical for the before and after Weather Enclosure cases.

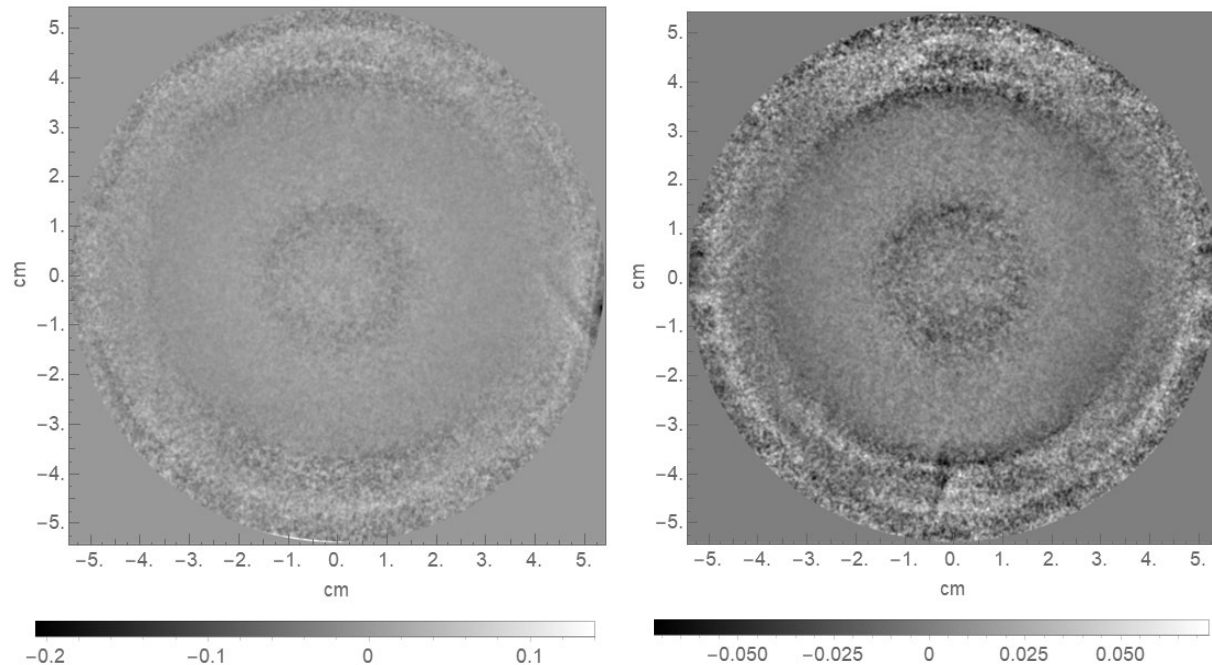


Figure 27: DARHT Axis 1 Collimator Calibrator residual images showing 3682 on the left and post weather enclosure on the right.

The simple conclusion from these analyses of the two data sets is that the DARHT radiographic system, which includes both accelerators and cameras, is essentially working identically as before the Weather Enclosure.

X. Summary Results and Conclusions

The summary results from this effort show that we have achieved equivalent shielding against spurious neutron and gamma-ray fluxes that interfere with DARHT radiographic image quality, but in the context of a space-constrained configuration of the new DARHT Weather Enclosure. Equally important, we have identified the significant residual pathways for neutron and gamma interference (it is primarily gamma). We have found that the neutron and gamma fields extend throughout the firing point area; there does not seem to be a significantly preferred direction. It appears that the improvement is roughly asymptotic with effort, so that the considerable effort did not produce a linear improvement but rather a diminishing improvement effect. However, it is comforting that we have performed an exhaustive study so that the level of interference is approximately equivalent to the case with the heavy steel enclosures used before the Weather Enclosure. Further, we may be able to use the knowledge here to improve the future image quality. Lastly and most importantly, the BIE analysis of the 3682 and post weather enclosure data sets show almost identical results indicating that the radiographic performance of the DARHT facility is maintained.

XI. References

1. Zanini, A., et. al., Phys. Med. Biol. **49** (2004) 571–582
2. D. Binder, E. C. Smith and A. B. Holman, "Satellite Anomalies from Galactic Cosmic Rays," in *IEEE Transactions on Nuclear Science*, vol. 22, no. 6, pp. 2675-2680, Dec. 1975, doi: 10.1109/TNS.1975.4328188.
3. "Neutron-Induced Single Event Upset (SEU) FAQ", Microsemi Corporation, October 7, 2018, https://www.microsemi.com/document-portal/doc_download/130760-neutron-seu-faq
4. "MCNP User's Manual, Code Version 6.2," October 2017, LA-UR-17-29981, LANL.
5. International Tables for Crystallography, Vol. C
6. van Dokkum, Pieter G., Bloom, J., and Tewes, Malte, "L. A. Cosmic: Laplacian Cosmic Ray Identification". Astrophysics source Code Library, record ascl:1207.005. July 2012.